Journal of ELECTRONIC MATERIALS, Vol. 48, No. 9, 2019
https://doi.org/10.1007/s11664-019-07366-5
© 2019 The Minerals, Metals & Materials Society

Thermoelectric Generators Fabricated from Large-Scale-Produced Zr-/Hf-Based Half-Heusler Compounds Using Ag Sinter Bonding

DENNIS ZILLMANN,[1] DAVID METZ,[2] BARBARA MATHEIS,[2] ANDREAS DIETZEL,[2] ANDREAS WAAG,[1,3] and ERWIN PEINER[1,3,4]

1.—Institute of Semiconductor Technology (IHT), Technische Universität Braunschweig, Hans-Sommer-Str. 66, 38106 Brunswick, Germany. 2.—Institut für Mikrotechnik (IMT), Technische Universität Braunschweig, Alte Salzdahlumer Str. 203, 38124 Brunswick, Germany. 3.—Laboratory for Emerging Nanometrology (LENA), Technische Universität Braunschweig, Langer Kamp 6a, 38106 Brunswick, Germany. 4.—e-mail: e.peiner@tu-bs.de

In this study, we present a fabrication process of thermoelectric (TE) power generator modules (TEGs) using the Ag sinter bonding technique for assembling the TE legs with their interconnecting bridges. As TE material, we use commercial half-Heusler (HH) compounds (p-type $Hf_{0.5}Zr_{0.5}CoSn_{0.2}Sb_{0.8}$ and n-type $Hf_{0.6}Zr_{0.4}NiSn_{0.98}Sb_{0.02}$), which offer high TE figures of merit in the medium-to-high temperature range. Magnetron-sputtered bilayers of Au and TiW are deposited on top of the TE legs as metallization and diffusion barriers, respectively. Stability of the sinter-bonded joints is investigated by application of external tensile stress and thermal stress by cyclic temperature change followed by an analysis of the fracture surfaces. As the main cause of failure, we reveal a mixed pattern of near-surface cracking in the HH compounds and adhesion fractures between the sinter layer and the thin-film metallizations. Fabricated two-leg and four-leg unicouple TEGs are operated at maximum temperature differences of 325 K and 400 K across the TE legs, respectively, and maximum hot-side temperatures of 375°C and 510°C, respectively. The resulting maximum power densities amount to 1.0 W cm^{-2} (two-leg) and 1.9 W cm^{-2} (four-leg), and for the TE figures of merit, we calculate 2.6×10^{-4} K^{-1} (two-leg) and 3.4×10^{-4} K^{-1} (four-leg).

Key words: Thermoelectric modules, TEG, Seebeck effect, half-Heusler compounds, silver powder, Ag sinter joining technique, TiW, diffusion barrier, contact resistance, internal resistance, tensile strength

INTRODUCTION

Thermoelectric (TE) power offers a way to recover waste heat from industrial processes or transportation by converting heat directly into electricity.[1,2] In addition to high performance (indicated by a large TE output power, conversion efficiency, etc.), volumetric cost (material cost, fabrications cost, etc.) is the key factor on the way to make TE competitive for waste heat recovery with conventional methods. In this context, toxicity, abundance, and cost of TE materials have to be considered, but also appropriate methods of large-volume manufacturing of TE legs and their assembly into TE generator modules (TEGs).

At medium-low temperatures, bismuth telluride is established not only for TE cooling applications but also for TE waste heat recovery. For the latter, a conversion efficiency of η = 7.2% was reported in a 9-kW heat recovery system.[3] It consisted of BiTe

(Received March 4, 2019; accepted June 7, 2019; published online June 20, 2019)

TEGs operated at a temperature gradient of $\Delta T = 250$ K and a maximum temperature applied to the hot side of the TEG of $T_h = 280°C$. For the medium-high-temperature range (up to $T_h = 500°C$), PbTe-based materials are better suited. A conversion efficiency of 6.56% ($P_m = 1.824$ W) at $\Delta T = 360$ K and $T_h = 400°C$ was achieved with commercial segmented-leg PbTe modules from Tellurex Corporation.[4] As lead-free, low-cost alternatives for this temperature range, skutterudites and half-Heusler (HH) compounds are expected to be commercialized soon.[5] A conversion efficiency of 7% and an output power of 10.5 W per module at $\Delta T = 460$ K and $T_h = 500°C$ were reported for a skutterudite-based TEG using materials produced in kg amounts.[6] Meanwhile, skutterudite powders are offered in production quantities of more than 500 kg per year from Treibacher Industrie GmbH, Althofen, Austria.[5]

Manufacturing and testing of TEGs was also reported for HH compounds, which were produced in volumes from 1 kg to 7 kg and show $\eta = 5\%$ and $P_m = 2.8$ W per module at $\Delta T = 527$ K and $T_h = 550°C$.[7] Recently, Isabellenhütte Heusler GmbH, Dillenburg, Germany, announced a process for HH bricks/wafers in amounts of 10 kg per production run, which is claimed to be up-scalable to 25 tons per year.[8]

Besides issues of TE performance (like stability, conversion efficiency, etc.) and production in large quantities, TEG assembly is an important factor related to the final cost of TE energy conversion. According to their different maximum operation temperatures, BiTe-, PbTe-, skutterudite-, and HH-based TEGs conventionally use high-temperature soldering, direct bonding, brazing, or fast hot pressing, respectively, for bonding TE legs with their interconnecting metal bridges. The melting point of the bonding material is adapted to the maximum operation temperatures. It ranges from 350°C for high-temperature PbSnAg solder[9] to more than 600°C for direct bonding using Ni, Co, or NiFeMo foils in a hot press.[10] For a stable contact to HH compounds at temperatures of > 600°C, Ag was proposed as a potential candidate owing to its excellent electrical and thermal conductivity.[11] Using hot pressing at 40 MPa and 780°C under vacuum, a contact resistivity of 38 $\mu\Omega$ cm^2 to 89 $\mu\Omega$ cm^2 and 339 $\mu\Omega$ cm^2 to 91 $\mu\Omega$ cm^2 was reported between RT and 500°C for p-type and n-type HH compounds, respectively. A much lower contact resistivity of ~ 1 $\mu\Omega$ cm^2 was obtained with a HH TEG metallized by Ti foil using hot pressing at 600°C to 800°C, which can generate a power density of 8.9 W/cm^2 at $\Delta T = 678$ K.[12]

Compared to hot pressing and brazing, sinter bonding is typically performed at much lower pressure and temperature. No liquid-phase transition is necessary during the bonding process, thereby hindering the formation of intermetallic phases or an unstable reaction layer. For sinter bonding of TE devices, a commercial pick and place setup was proposed (Fineplacer Pico, Finetech, Berlin, Germany)[13] and validated by fabrication and testing of BiTe TE micro-coolers (μTECs) and TEGs.[14–16] μTECs consisting of Au/Ni-coated BiTe legs, which were sinter-bonded at 5.5 N/mm^2 and 250°C to 270°C, offer much higher maximum operating temperatures ($T_h = 300°C$) compared to Sn-Sb-soldered commercial devices.[14] They show good cycling stability and a low specific contact resistance of $\rho_c = 14 \pm 1$ $\mu\Omega$ cm^2. Ag-sinter-bonded BiTe TEGs (at 5 N/mm^2 and 270°C with $N = 20$ legs) on Cu interconnects were operated up to maximum temperatures of $\Delta T = 300$ K and $T_h = 350°C$.[15] This is considerably higher than the values reported for commercial modules ($\Delta T = 250$ K and $T_h = 280°C$).[3] Measured contact resistivities of $\rho_c = 2100$ $\mu\Omega$ cm^2 to 2700 $\mu\Omega$ cm^2 were yet high, but could be reduced to $\rho_c = 50 \pm 30$ $\mu\Omega$cm^2 using BiTe legs with an 8-μm-thick Ni diffusion barrier.[16]

Sinter-bonded interconnects were also used for nanocrystalline bulk silicon synthesized using nanoparticles from a fully scalable production process.[17] Here, sinter bonding assembly of TEGs was done using Ag paste at 300°C for 1 h on a Ni/NiSi metallization. In spite of the low bonding temperature, the fabricated TEGs were operated up to $\Delta T = 300$ K and $T_h = 600°C$ yielding a maximum output power of $P_m = 1$ W per module at very low contact resistances of $\rho_c < 1$ $\mu\Omega$ cm^2.[17] It was concluded that silver sintering can be a method for future large-scale manufacturing of TE devices, since it may better compensate for small deviations in the height of TE legs than other methods.[18] A higher contact resistivity of several hundreds of $\mu\Omega$ cm^2 was reported for PbTe-based TE legs sinter-bonded using nano-silver paste.[10] In this case, a Ni barrier layer was effective to impede the diffusion of Ag into the TE leg at 400°C, but diffusion of Cu from the interconnect layer and Ni itself into the TE leg led to a notable reduction of the Seebeck coefficient. A better diffusion barrier layer was postulated to be necessary for stable TEG operation at 500°C.

In this work, we describe the application of Ag sinter bonding for the assembly of TEGs based on half-Heusler (HH) compounds. First, the deposition process of a suitable contact metallization is depicted including a diffusion barrier layer, which is necessary to prevent reactions between the HH compound and the sinter joint at medium-high temperatures. We select TiW, which was reported to be an effective barrier layer against silver diffusion at temperatures up to 600°C.[19] Subsequently, the design of two-leg and four-leg unicouple TEGs is delineated based on commercially purchased HH pellets of $Hf_{0.5}Zr_{0.5}CoSn_{0.2}Sb_{0.8}$ (p-type) and $Hf_{0.6}Zr_{0.4}NiSn_{0.98}Sb_{0.02}$ (n-type).[20] These modules are then assembled using Ag sinter bonding in a process (pressure, temperature, and time) adapted to the brittleness of the HHs based on our experience with telluride-based TEGs and TECs.[13–16]

Performance of the first TE modules (internal resistance, Seebeck voltage) in the medium-high-temperature range (at ΔT up to 400 K and T_h up to 510°C) is addressed as well as the effect of the related thermal stress on the sintered interconnects. Failure mechanisms are investigated with TEGs loaded by thermoshock and externally applied tensile stress. Based on the results of this study, the basic suitability of silver sinter bonding for manufacturing TEGs based on commercial HH compound material shall be evaluated. Remaining shortcomings and strategies for improvement will be discussed.

EXPERIMENTAL PROCEDURES

TiW Layer Deposition and Characterization

We first deposited TiW at various thicknesses (10 nm to 600 nm) on cleaned silicon or glass substrates. Ar-based DC magnetron sputtering (LS 440S, Ardenne Anlagentechnik, Oederan, Germany) was used from a sputter target composed of 10 wt.% Ti and 90 wt.% W (99.95% purity) at a background pressure of 10^{-6} mbar. We observed a linear dependence of the deposition rate on the DC power (Fig. 1). Composition and crystal structure of deposited TiW layers were determined by energy dispersive x-ray spectroscopy (EDX) and by x-ray diffraction (XRD, $\lambda = 0.15406$ nm), respectively. EDX measurements were done with a 600-nm-thick layer on glass using the built-in detector (X-Max, Oxford Instruments, UK) of a scanning electron microscope (SEM, Zeiss Supra VP40, Carl Zeiss, Germany). For XRD with 200-nm-thick layers on glass, a diffractometer at an incident x-ray angle of 5° (Empyrean, PANalytical, UK) was utilized. Furthermore, a self-built, four-point-probe setup was employed to measure the electrical resistivity of the deposited layers at temperatures from RT to 300°C at a heating rate of 7 K/min. For these measurements, a reduced oxygen atmosphere ($< 1\%$ O_2) was realized by a leak-proof box flushed with N_2 gas. The surface of the as-deposited TiW layers was analyzed using x-ray photo-electron spectroscopy (XPS, resolution of < 0.5 eV) using an Omicron NanoSAM (Scienta Omicron GmbH, Germany).

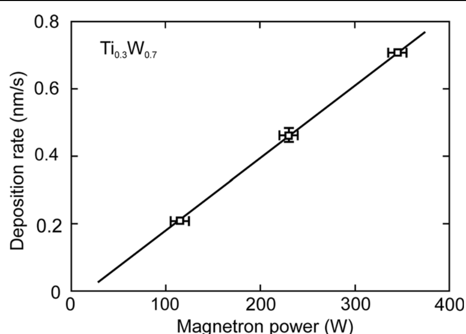

Fig. 1. Deposition rate of TiW in dependence on DC sputtering power using Ar gas and a $Ti_{0.3}W_{0.7}$ target (10 wt.% Ti, purity of 3 N) at a background pressure of 10^{-6} mbar.

Composition, Crystallinity, Surface States, and Resistivity of the TiW Layers

Repeated EDX point spectra of a 600-nm-thick TiW layer deposited at 345 W (Fig. 2a) revealed a layer composition of 91.8 ± 0.2 wt.% of tungsten and 8.2 ± 0.2 wt.% of titanium. This is slightly different from the composition of the target (10 wt.% Ti). A correspondingly lower titanium content in sputter-deposited TiW layers with respect to the target composition was already reported before.[21] It was related to the different stopping behavior of Ti and W atoms in the Ar gas during the sputter deposition process.

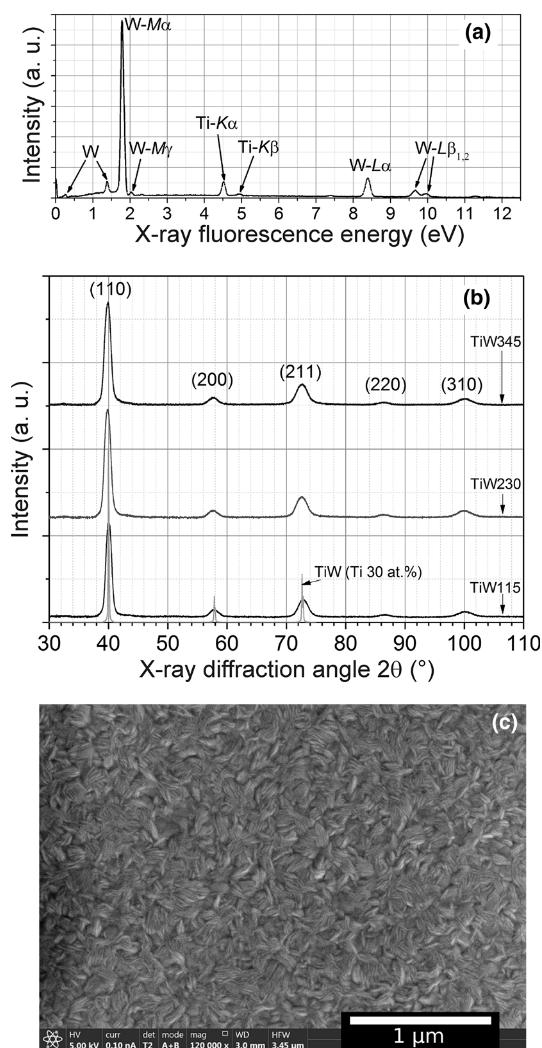

Fig. 2. TiW layers on glass analyzed by EDX (a, deposited at 345 W) and by XRD (b, deposited at 115 W, 230 W, and 345 W). EDX revealed the composition (W: 91.8 ± 0.2 wt.%, Ti: 8.2 ± 0.2 wt.%) and XRD revealed the crystallization of a homogeneous phase ($\alpha-$W with 30 at.% of dissolved Ti). The SEM photograph (c) exhibits elongated sub-micron-sized features which we assigned to TiW grains.

The XRD measurements with TiW were analyzed based on iterative Rietveld refinements using pseudo-Voigt profiles to estimate the precise positions of the Bragg reflections (Fig. 2b). It turned out that the TiW layers crystallized in the cubic α phase of W with a lattice constant of 0.3182(5) nm, corresponding to an amount of ~10 wt.% of solved Ti (see EDX). The broadening of the reflections indicates a polycrystalline structure of sub-micron grain size. The SEM image in Fig. 2c revealed surface features having elongated shapes of $\sim$ 200 nm in length and of several tens of nanometers in width, which roughly matches to the sub-micron grain size found by XRD. Correspondingly, a fiber-like poly-crystalline structure of sputter-deposited TiW was reported.[22]

XPS measurements were performed on both as-deposited TiW layers exposed to normal atmosphere at RT and on subsequently sputter-cleaned TiW. On TiW layers exposed to normal atmosphere, peaks assigned to oxide states (TiO_2 and WO_3) were observed in addition to the metallic Ti and W bonding states.[23] After a subsequent sputter etching step, the oxide-related peaks in the XPS strongly weakened or entirely vanished from the spectrum.

Consequently, to protect the TiW layer from oxidation and as a necessary adhesion promoter for the sinter bonding, a noble-metal layer had to be deposited on the TiW immediately after, without breaking the vacuum in the sputter chamber. Following our experience with sinter bonding of small dies (silicon, III/V compounds, tellurides), we selected Au for this purpose.[13–16,24,25] Thickness and conformity of the TiW diffusion barrier layer on HH pellets were carefully considered to avoid/minimize diffusion of Sn into the Au top metallization. Sn might segregate from the HHs at 231°C as observed recently by differential scanning calorimetry (DSC) but not by XRD.[20] This is an important issue regarding the reactivity of Sn with Au as detailed in the next section as well as in Sect. 3a and c.

Electrical resistivity ρ of TiW measured by a four-point probe exhibited a value of 0.73 ± 0.02 $\mu\Omega$ m at 40°C, which increased slightly to 0.81 ± 0.02 $\mu\Omega$ m at 300°C. These results are in good agreement with a reported value of 0.8 $\mu\Omega$ m.[22] Obviously, this value is much smaller than the resistivity of the p-type and n-type HH compounds (5 $\mu\Omega$ m to 80 $\mu\Omega$ m[20]); i.e., its contribution to the module resistance was neglected.

TiW Diffusion Barrier on HH Compounds

TE pellets from HH compounds having a geometry of $3 \times 2.5 \times 2.5$ mm^3 were purchased from Vacuumschmelze GmbH & Co. KG (Hanau, Germany). Height and roughness were measured using a micrometer and a confocal microscope (μsurf custom, NanoFocus AG, Germany), respectively. We found an average value of 3000 ± 5 μm for the height and an area-related surface roughness ranging from 0.59 μm to 1.77 μm. The pellets were cleaned in an ultrasonic bath using isopropanol and were subsequently etched for 1 min using aqueous hydrofluoric acid solution (HF, 40 vol.%) for better adhesion of the TiW diffusion barrier layer. A 200-nm-thick TiW layer was sputter-deposited at a power of 345 W (i. e., a deposition rate of 0.71 nm/s) on the TE legs. Without breaking the vacuum, we then deposited a 500-nm-thick Au layer on the TiW using a power of 200 W. The noble-metal surface finish on top of the TiW layer was found to be necessary to obtain strongly adhesive joints using the following Ag sinter bonding process.[13–16]

Figure 3 shows in a top-view SEM photograph a HH pellet covered by an Au/TiW bilayer revealing an open-pored surface morphology, which is very similar to the surface of Fe-doped ZrCoSb HH compounds by arc melting.[26] In our case, the HH pellets were manufactured by a sequence of melting, powder milling, and sinter compaction as described in detail previously.[20] Conformal covering of the HH pellet by the Au/TiW bilayer was indicated by good adhesion as confirmed by peeling tests using Scotch tape. Here, further support was provided by cross-sectional SEM with a TEG after high-temperature operation addressed in Sect. 3c. Only a few pinholes are visible in the bilayer, and they are correlated to near-surface cracks in the HH compounds, which evolved upon the high-temperature treatment.

Sinter Bonding Process

Sinter bonding was performed using a powder of flake-like Ag particles (silver flake 70a, Ferro GmbH, Germany). Alumina ceramic substrates ($13 \times 9 \times 0.63$ mm^3, CeramTec GmbH, Germany) with burnt-in Ag pads ($3 \times 7 \times 0.02$ mm^2, resistivity: $\sim$ 0.03 $\mu\Omega$ m) were employed as interconnecting bridges between the metallized TE legs. A Fineplacer Pico (Finetech GmbH, Berlin, Germany) was used for pick and place handling of the legs as well as the sinter bonding at defined pressure and temperature.[24] This process is illustrated in Fig. 4,

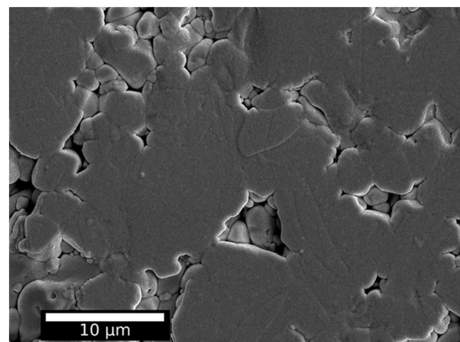

Fig. 3. SEM photograph of a p-type HH ($Hf_{0.5}Zr_{0.5}CoSn_{0.2}Sb_{0.8}$) TE leg covered by a Au (500 nm)/TiW (200 nm) bilayer stack.

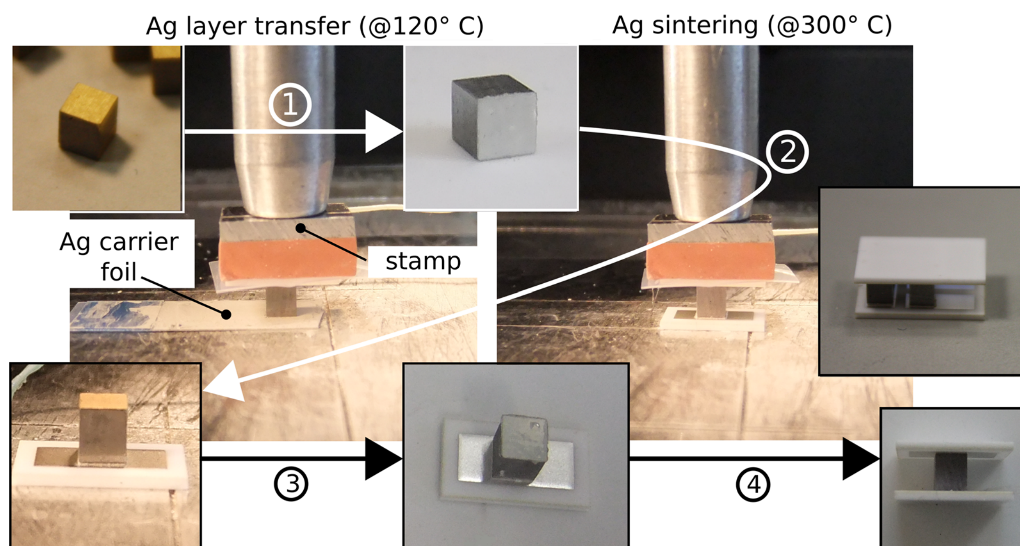

Fig. 4. Fabrication process of sinter-bonded connections between HH TE legs and ceramic plates using a Fineplacer Pico (Finetech GmbH, Berlin, Germany). In step 1, a silicone stamp is employed for picking a metallized HH leg and pressing it onto a carrier foil, where a pasty layer of Ag powder is transferred to the leg (120°C, 6 MPa, 1 min). In step 2, the leg with the pasty layer is pressed onto the Ag pad of a ceramic plate for sinter bonding (270°C to 300°C, 6 MPa, 5 min to 10 min). In steps 3 and 4, the TE module is completed by repeating steps 1 and 2 with the already connected leg-bridge assembly using the same parameters, respectively, as above.

exemplarily with a one-leg module, which is representative also for the fabrication of two-leg and four-leg modules. First, Ag powder is mixed with ethanol to form a paste, which is then screen-printed in a thickness of 20 μm to 50 μm to a temperature-stable carrier foil and dried for 1 h at RT to expel the solvent. Subsequently, a TE leg is picked using the stamp of the Fineplacer Pico and pressed onto the foil for 1 min at 6 MPa and 120°C, thereby transferring a part of the pasty layer to the leg surface.[24] The temperature of 120°C is low enough to prevent the Ag paste from early sintering. Finally, the leg is placed onto the Ag pad of an alumina substrate and sinter bonded at a pressure of 6 MPa and temperature of either 270°C or 300°C under normal atmosphere conditions for 5 min to 10 min.

The sintering parameters (pressure, temperature, time) were chosen based on experience with sinter bonding of various semiconductor materials including silicon (power electronics, MEMS), GaN (LEDs), GaP (photo-diodes), and BiTe (TE devices).[25] The best sintering results were normally found using high pressure (10 to 20 MPa) and hard stamps (steel, PEEK). However, in the case of fragile components (large IC dies, MEMS) or brittle materials (BiTe), a soft silicone stamp had to be used at reduced pressure (4 to 5.5 MPa) to avoid damage to the dies. To maintain sufficient sintering, we therefore increased the process temperature to 270°C to 300°C and the process time from 2 min to 5 min.

In Fig. 5, SEM photographs of Ag paste transferred on a TE leg are depicted before (a) and after (b) sintering at 6 MPa, 300°C, and 5 min. Sinter necks formed between the flakes ($<$ 10 μm) of silver powder, confirming the onset of sintering. However,

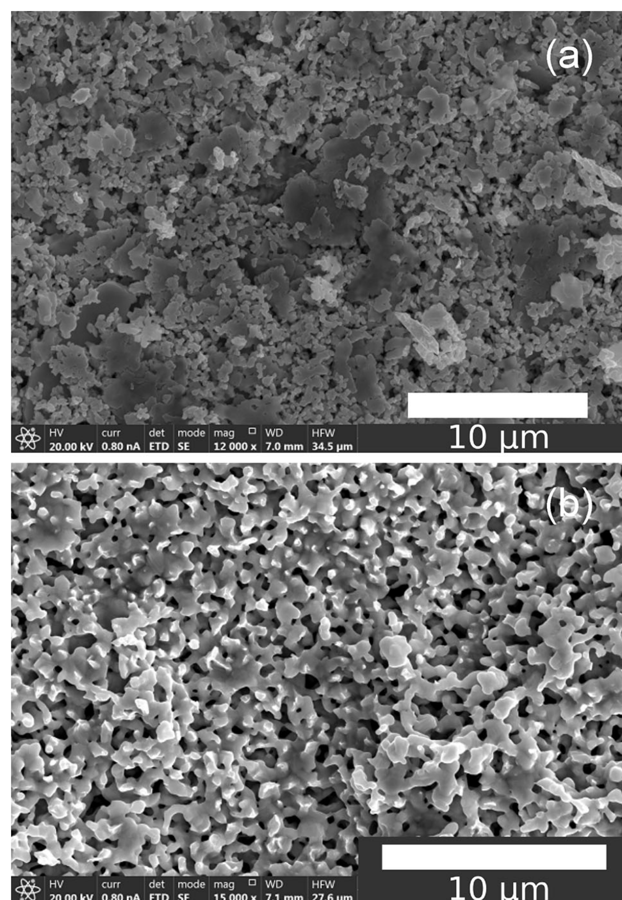

Fig. 5. Ag powder (SF 70a, Ferro GmbH, Frankfurt, Germany) transferred at 6 MPa and 120°C for 1 min onto a HH (a) leg and after sintering at 6 MPa and 300°C for 5 min (b).

rather large pores remained between the sinter necks, indicating incomplete sintering of the Ag flakes. Incomplete sintering by different thickness and non-uniformity of the printed silver paste and non-uniform pressure by a flexible silicone rubber stamp was reported as a reason for reduced shear strength of Ag-sinter-bonded SiC dies on direct-copper-bonded (DBC) substrates.[27] However, the damage patterns detailed in Sect. 3b, did not reveal cohesive fracturing of the sinter layer as the reason for failure of our TEGs, indicating an acceptable selection of the sintering parameters.

Figure 6 shows in its upper part a photograph of a realized four-leg TE module in a sandwich architecture, where the *p*-type und *n*-type TE legs are connected in series via Ag pads alternately on the upper and the lower ceramic plates (cf. lower part of this figure).

TEG Characterization

Measurements of the mechanical tensile strength of the sinter connections were carried out with one-leg modules of both *n*-type and *p*-type HH compounds. In view of the brittleness of HH compounds, we did not use shear testing, which held the risk of cracking the leg, if the tool was not well-aligned. Instead, we decided to employ tensile testing, which is also state of the art for evaluating silver sinter bonding with an almost identical tendency of deformation behavior as shear testing.[27]

Tensile testing was done by applying a vertical uniaxial force to one-leg TE modules. For this, the modules were inserted in the clamping device of a tensile tester (ZwickRoell GmbH and Co. KG, Germany). Two specially designed stainless-steel adaptors were used to accommodate the ceramic substrates and to prevent cracking induced by the clamping. Tensile stress was applied to the legs of a contact area of $A = 2.5 \times 2.5\ \mathrm{mm}^2$ and a height of 3 mm. Force was increased in steps of 1 N, which was measured using a 200-N load cell at a resolution of 0.1%. Unfortunately, fracture occurred already after the first few loading steps. Thus, information on the viscoelasticity of the joint, e.g., from load-displacement curves, could not be obtained. The fracture surfaces were then analyzed using SEM and EDX.

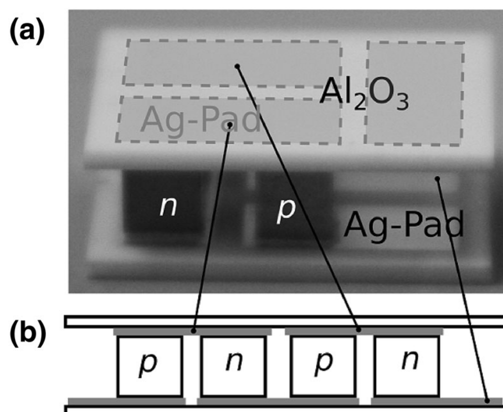

Fig. 6. Photograph of a fabricated four-leg TEG (a) and schematic of the electrical series connection of the legs (b).

For evaluating the TE performance of the fabricated HH modules, the temperature dependence of the internal resistance R_i and the Seebeck voltage U_th were measured. In the case of R_i measurement, one-side heating of the TEG was done from RT to 200°C at a rate of 7 K/min, and the voltage drop across the TEG by an injected current of (400 ± 10) mA was measured. For electrical connection of the TEGs, we attached copper wires to the Ag contact pads on the ceramic substrates using Sn-based solder, so the maximum applied temperature had to be limited to 200°C. A four-point probe arrangement was selected to cancel out the voltage drop across the Cu wires; i.e., the probe current was fed into the device through one pair, and the resulting voltage drop was recorded using the other. For temperature measurement, type *K* thermocouples were fixed applying silver conducting paste to the Ag pads on the alumina substrates of the module.

Measurements were done for each temperature step in time intervals of 20-s duration, during which current was injected for 12 s and then switched off for 8 s. During the 8 s, when the probe current was switched off, the parasitic Seebeck voltage superimposed to the ohmic voltage drop was measured. Furthermore, the interruption of the current injection after 12 s was expected to minimize the effects of Peltier and Joule heating in the TEG. A negligible hysteresis visible in the voltage measurements (corrected for the Seebeck voltage) between heating and cooling cycles supported this assumption.

Seebeck voltages were measured up to $T_\mathrm{h} = 510$°C. To prevent oxidation at these higher temperatures, compared to 200°C for the R_i measurements, the TEG was operated in a protective nitrogen atmosphere ($\sim O_2$ partial pressure of ~ 1 kPa). Furthermore, the temperature-limited soldered Cu wire connections were placed not on both sides but only on the cold side of the module, where temperatures of 50°C to 100°C were sustained by a water-cooled CuZn block.

For the measurement of the Seebeck voltage, the effective temperature difference between the hot and the cold side of the TEG had to be determined. As before, we positioned the thermocouples for temperature measurement on the Ag pads of ceramic substrates. Thus, the temperature drop over the ceramic substrates and the contacts between the module and the heat source/sink were not included in ΔT. To evaluate the resulting deviation we estimated the thermal resistance of the ceramic substrates and the thermal contact resistance between the substrate and the heat source/sink. For the alumina substrates $(13 \times 9 \times 0.63\ \mathrm{mm}^3)$ with a thermal conductivity

of ~ 25 W/K/m, we determined a thermal resistance of ~ 0.22 K/W. The thermal contact resistance depends on surface roughness and hardness of the contacting solids and, eventually, an applied contact pressure or thermal grease.[28] In our case, we mounted the TEG on a hot plate as heat source and used a water-cooled CuZn block on top as heat sink and contact load (~ 5 N). We found good thermal coupling, which could not be further improved using graphite thermal pads put between the contacting solids. Assuming a joint thermal resistance of ~ 2 cm^2K/W, which can be expected for a typical ceramic package assembly on a heat sink at the applied contact pressure of ~ 43 kPa, we can estimate a gap thermal resistance of ~ 1.7 K/W.[28] The total thermal resistance by the substrates and the contacts amounted therefore to ~ 4 K/W, which is much smaller than the thermal resistance of the TEG legs of R_{th} ~ 53 K/W (two legs) and ~ 26.5 K/W (four legs). The resulting underestimation of the effective temperature difference over the TEG (by 8% to 15% of R_{th} of the two-leg and the four-leg TEG, respectively) may thus be acceptable, but was taken into account when discussing TE performance with respect to published results.

During the Seebeck voltage measurements, one four-leg TEG was treated unintentionally by uncontrolled fast cooling down (>> 10 K/min, thermoshock) leading to immediate failure by fracture at its hot-side joint. The fracture surfaces of TE leg and ceramic substrate were analyzed using SEM and EDX.

RESULTS AND DISCUSSION

Thermal Stability of Metallization

Before module fabrication, thermal stability of the Au/TiW metallization stack on the HH compounds was investigated using EDX. For this, a 1-h temperature treatment at 500°C without control of temperature increase/decrease rates was done in a nitrogen-flushed muffle furnace at atmospheric pressure. Furthermore, differential scanning calorimetry (DSC) was performed with selected HH samples (of mass < 80 mg) using a Netzsch DSC 204 F1 Phoenix (Netzsch-Gerätebau GmbH, Selb, Germany). Under argon purging (gas flow of 20 mL/min), heating and cooling rates of 10 K/min and a 10-min constant temperature plateau at 500°C in between were set. The specific heat capacity c_p was determined using the ratio method and sapphire as the reference, resulting in $c_p(T)$ curves of *n*-type and *p*-type HHs as shown recently.[20]

Temperature treatment in the muffle furnace led to a color change from golden to silver-colored related to agglomerations of Au and Sn, which were analyzed in spot checks by EDX. Here, mostly atomic concentration ratios of Sn to Au of 50:50 were found corresponding to the composition of the δ phase of AuSn. We assume that molten Sn from the HH surface penetrated through pinholes in the TiW to the top Au metallization leading to liquid solutions of Au and Sn. During the cooling process, possibly, crystallization to intermetallic phases had occurred (ζ and δ) according to the Au-Sn phase diagram. DSC analyses with metallized HH compounds, however, revealed only an endothermal reaction at 231.9°C (related to the melting of pure Sn[20]), but no reaction signature was visible at the melting point of the δ phase at 419.3°C. We conclude, that the formation of pin holes in the TiW layer leading to penetration of Sn and reaction with Au only occurred under rapid heating/cooling. At controlled heating/cooling rates of less than 20 K/min, this detrimental effect played a minor role as shown by the DSC measurements.

In this context, we investigated the effect of unintentional uncontrolled fast cooling treatment (>> 10 K/min) of the hot side of a TE module, which led to immediate failure. Here, fast thermal stress generation was expected in the Ag layer with its much larger thermal expansion coefficient of 19×10^{-6} K^{-1} with respect to the HH compounds (8.5 to 9.8×10^{-6} K^{-1})[20] and the alumina substrate (8×10^{-6} K^{-1}). The generated shock stress could not be relieved by relaxation processes and led to fracture of the hot-side interconnect of the TEG. Figure 7 shows cracks in the Ag sinter layer surrounding HH, which broke out of the pellet and adhered on the Ag pad of the detached ceramic plate.

Mechanical Stability of the TEG Modules

We then investigated the bonding strength of the sinter-bonded Ag-Au/TiW/HH system upon external stress application to one-leg modules of both *p*-type

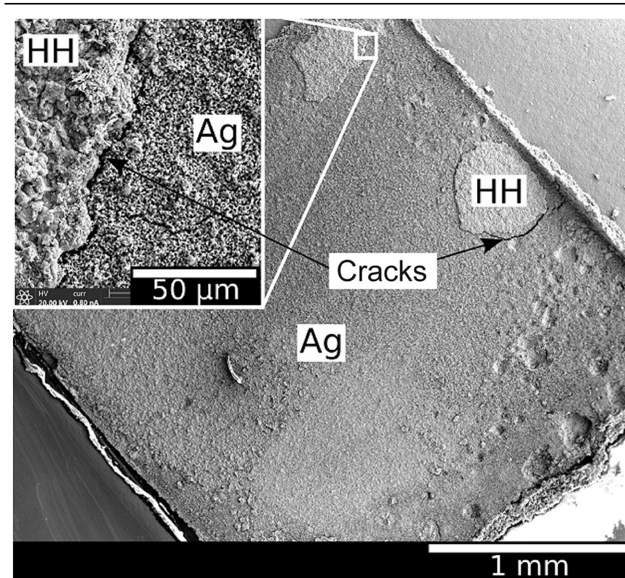

Fig. 7. SEM photograph of a hot-side Ag pad of a broken four-leg module after temperature-shock treatment. Cracks are visible in the Ag pads, e.g., close to adhering HH fragments (cf. Figure 8).

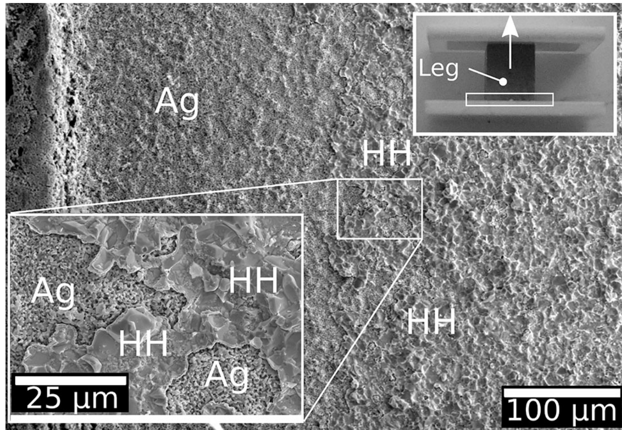

Fig. 8. SEM photograph of a broken one-leg TEG after uniaxial tensile loading showing a large amount of residues of the *n*-type HH compound adhering on the Ag pad of a ceramic plate. The upper inset shows a typical one-leg module for tensile strength testing (the direction of the applied force is indicated by the arrow).

and *n*-type HH compounds. We measured tensile fracture strengths between 1.3 MPa and 1.8 MPa, which are much lower than values of ~ 10 MPa to ~ 50 MPa to be expected by low-temperature and low-pressure sinter bonding.[27] An even higher tensile fracture strength of ~ 150 MPa was reported for a skutterudite-based TEG with brazed interconnects.[29] And for a sinter-bonded BiTe-based TEC, still a shear strength of 11 ± 1 MPa was obtained.[14] Furthermore, we expected strong adhesion of TiW to HH compounds according to the strong bonding strength of 50 MPa reported for hot-pressed Ti foils on HH legs.[12] To elucidate the observed premature failure, we carefully analyzed the fracture surfaces of the failed joints using SEM/EDX.

Mixed damage patterns were found for all specimens as visible in Fig. 8, where the fracture surface of the ceramic substrate of a broken device is shown. In addition to uncovered Ag we found extended regions with fragments of the HH compound adhering on the Ag pad. Using EDX, we detected traces of Au/TiW below these fragments but not on the uncovered Ag pads. We conclude that fracture mostly occurred in the near-surface region of the HH compounds. Corresponding patterns were found on the fracture surface of the HH leg showing uncovered HH compound, areas of Au with Ag residues, and regions of pure Ag. The latter two indicate poor adhesion of the sinter layer to the Au and Ag metallizations, respectively. In all cases, however, detaching of the Au/TiW bilayer from the HH compound did not occur. We relate the failure patterns to non-uniform pressure application during sinter bonding owing to the open-pored surface morphology of the HH legs combined with a non-uniform thickness of the sinter layer. We expect therefore, that a better surface preparation of the HH legs and smoother transfer of Ag paste will largely suppress these problems in the future.

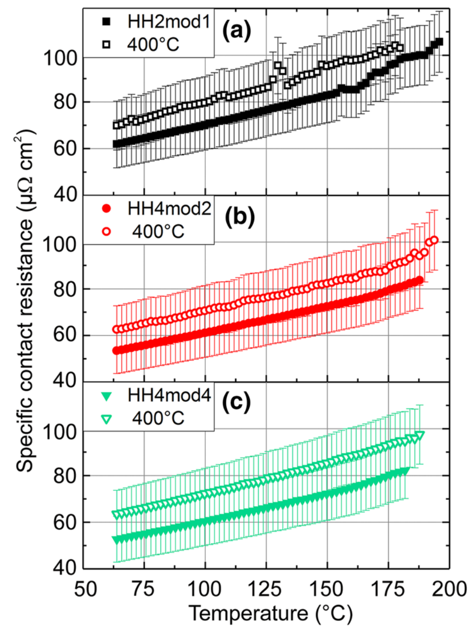

Fig. 9. Contact resistivity in dependence on temperature of a two-leg TEG (a) and two four-leg TEGs (b) and (c) calculated using $\rho_c = 2R_cA/N$ (number of legs: N, cross-sectional area: $A = 2.5 \times 2.5$ mm^2, contact resistance: $R_c = R_i - R_{np}$). R_i and R_{np} correspond, respectively, to the measured internal resistance and the average bulk resistance of *p*-type $Hf_{0.5}Zr_{0.5}CoSn_{0.2}Sb_{0.8}$ and *n*-type $Hf_{0.6}Zr_{0.4}NiSn_{0.98}Sb_{0.02}$ (cf. Ref. 20). Filled and open symbols refer to measurements before and after four to six temperature cycles to 400°C, respectively.

Nevertheless, the Au/TiW metallization exhibited in all cases strong bonding with the HH compounds, which was not affected by external tensile stress loading, confirming the effectiveness of TiW as an adhesion layer between the HH leg and the Au metallization.

Internal Resistance and Seebeck Voltage of the TEG Modules

We measured the internal resistances of three four-leg modules ($N = 4$) and one two-leg device ($N = 2$; cf. Sec. II.E). The corresponding internal resistance R_i showed a nearly linear increase from 20 mΩ at RT to 30 mΩ at 200°C for $N = 4$ and from 10 mΩ at RT to 15 mΩ at 200°C for $N = 2$. This is in agreement with a linear increase of R_i with ΔT up to 527 K reported for TEGs of HH compounds of the same compositions as in the present work brazed to Cu-based electrodes.[7] The average bulk resistances R_{np} of the *n*-doped and *p*-doped TE legs contributing to R_i were calculated from their dimensions and resistivities (cf. Ref. 20). According to $R_c = R_i - R_{np}$, we then obtained contact resistances of 7 mΩ to 14 mΩ ($N = 4$) and 3 mΩ to 7 mΩ ($N = 2$), respectively, which represented significant contributions to the internal resistances (~ 30% to ~ 50%). Using $\rho_c = 2R_cA/N$ with the cross-sectional area of a leg of $A = 2.5 \times 2.5$ mm^2, contact resistivities were calculated as displayed in Fig. 9. After multiple heat

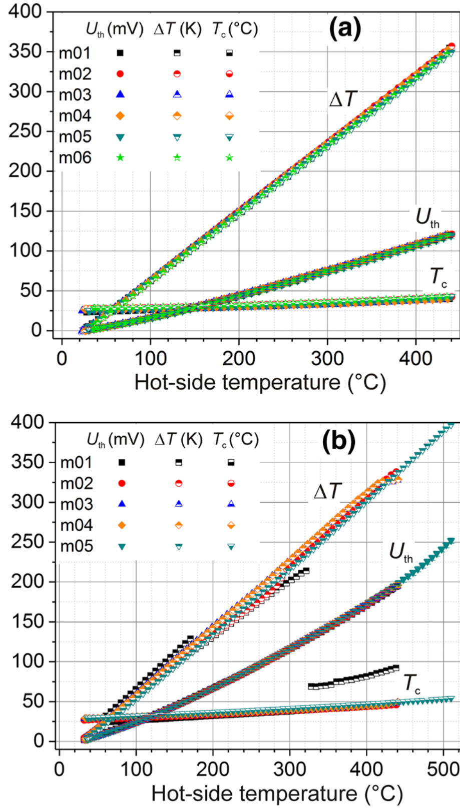

Fig. 10. Results of repeated measurements of Seebeck voltage U_{th}, temperature difference ΔT, and cold-side temperature T_c in dependence of the hot-side temperature T_h measured with a two-leg (a) and a four-leg TEG (b). The parameters on the ordinate are displayed using the same scaling; for the units, see the inset with the definition of the symbols.

treatments at $\sim$ 400°C (four times to six times for the investigated modules), we observed a slight increase of ρ_c by 10% to 20% (N = 4) and by 10% to 15% (N = 2). The resulting values of ρ_c ranged from $\sim$ 60 $\mu\Omega$ cm^2 to $\sim$ 100 $\mu\Omega$ cm^2.

Subsequently, we measured repeatedly the Seebeck voltage U_{th} of the TEGs for different hot-side temperatures T_h while keeping the cold-side temperature T_c at 50°C to 100°C. In Fig. 10, the results for U_{th} are displayed in dependence on T_h measured with a two-leg (a) and a four-leg TEG (b). We obtained reasonable reproducibility between the measurement runs, which were performed to different maximum values of T_h of up to 510°C. The maximum values of the Seebeck voltage were $U_{th,max}$ = 120 mV at ΔT = 352 K for the two-leg module and $U_{th,max}$ = 250 mV at ΔT = 400 K for the four-leg module.

For determining an estimate of the maximum module power P_{max} that could be generated under load-matching conditions ($R_L = R_{i,max}$), we employed the values of $U_{th,max}$ and the internal resistance $R_{i,max}$ at the applied maximum temperature gradient ΔT_{max}:

$$P_{max} = \frac{U_{th,max}^2}{4R_{i,max}} \quad (1)$$

By linear extrapolation of our measurements of R_i to ΔT_{max}, we found average values of $R_{i,max}$ = 18 mΩ and 33 mΩ for the two-leg and the four-leg modules, respectively. Thus, using the measured values of $U_{th,max}$ for both modules, we calculated a maximum module power of P_{max} = 0.2 W and 0.47 W for the two-leg and the four-leg module, respectively.

Table I shows a comparison of the resulting power densities with values reported for conventionally assembled TEGs for the medium-high temperature range as well as TEGs fabricated using sinter bonding. Obviously, the power densities of this study of 1.04 W cm^{-2} to 1.9 W cm^{-2} are higher than those of soldered or brazed skutterudite-based TEGs (0.75 W cm^{-2} to 0.9 W cm^{-2}), glued HH-based TEGs (0.28 W cm^{-2}), as well as sinter-bonded nanocrystalline silicon and telluride TEGs (0.18 W cm^{-2} to 0.93 W cm^{-2}). However, much higher power densities were reported for HH-based TEGs assembled by brazing (3.2 W cm^{-2}) and hot pressing (8.9 W cm^{-2}). We assign the lower power density P_{max}/NA of our devices partly to a lower Carnot efficiency corresponding to the lower ΔT_{max} ($\leq$ 400 K) we applied. Nevertheless, the full potential available for TEGs based on HH compounds was by far not yet exploited by our approach. We assign this to the high contact resistivity we achieved by sinter bonding. A reduction to 1 $\mu\Omega$cm^2 will be necessary, which might be realistic, as it was demonstrated with sinter-bonded silicon TEGs.[17]

According to Ref. 7, we further calculated a figure of merit using

$$z_m = \frac{R_{th}}{R_{i,max}} \frac{U_{th}^2}{(\Delta T_{max})^2} = \frac{4R_{th}}{(\Delta T_{max})^2} P_{max} \quad (2)$$

and the previously measured thermal conductivities of the p-type and n-type HHs[20] (yielding thermal resistances $R_{th} \approx$ 53 K/W and 26.5 K/W of the two-leg and the four-leg TEGs, respectively). We found figures of merit of our modules amounting to $z_m \approx 2.6 \times 10^{-4}$ K^{-1} to 3.4×10^{-4} K^{-1}, corresponding to maximum values of $ZT_{avg} = z_m(T_h - \Delta T_{max}/2)$ of 0.13 to 0.18. The values of z_m are only slightly lower than $z_m = 3.7 \times 10^{-4}$ K^{-1} reported for a TEG with HH legs of the same compositions as in the present study but assembled using brazing.[7] However, the values of the equivalent material figure of merit zT of 0.60 and 0.93 at 600°C for the used p-type and n-type HH compounds were much higher,[20] indicating the adverse effect of electrical contact resistance on the TE performance of our TEGs.

The temperature drop over the ceramic substrates and the contacts between them and the heat source/sink were neglected in the measurement of the temperature difference over the TE modules, resulting in an underestimation of the total ΔT across the TEG. On the other hand, the contributions of substrate and contact thermal resistances

Table I. Comparison of TE modules: number of TE legs N, $\Delta T_{max} = T_{h,\,max} - T_c$, with maximum hot-side temperature $T_{h,\,max}$ and cold-side temperature T_c, contact resistivity ρ_c, maximum generated power density per area of TE material P_{max}/NA, figure of merit z_m

Material	Bonding technology	N	Size (mm^3)	ΔT_{max} (K)	$T_{h,\,max}$ (°C)	ρ_c ($\mu\Omega cm^2$)	$P_{max}/(NA)$ ($W\ cm^{-2}$)	z_m ($10^{-4}\ K^{-1}$)	Ref.
Conventional bonding TEG assembly									
Skutterudite	Soldering using PbSnAg at 350°C	18	1.7 × 1.7 × 2.2	448	~ 473	~ 10[a]	0.9	–[b]	9
	Brazing to Al	64	4 × 4 × 4	470	500	~ 30	0.75	–[b]	29
HH	Gluing to Au/Ag using Ag paste	4	2 × 2 × 4	565	595	–[b]	0.28	0.3	7, 30
	Brazing to Cu bridges	14	2.5 × 2.5 × 3	527	547	1.0	3.2	3.7	7
	Hot pressing of Ti foil at 600 to 800°C	2	2.5 × 2.5 × 2	678	–	~ 1	~ 8.9	–	12
Ag sinter bonding TEG assembly									
Si, nano-crystalline	Sintering to DCB at 300°C	64	1.9 × 1.9 × 2.7	300	600	< 1	0.28[c]	–[b]	17
BiTe	Sintering to Cu bridges	20	1.5 × 1.5 × 1.0	320	350	2700[a)]–2100[d]	0.18[e]	0.8[f]	15
		2	1.4 × 1.4 × 1.0	190	250	~ 50	0.93[e]	–[b]	16
PbTe, n-type	Sintering to Cu electrodes	1	4 × 4 × 4	–[b]	RT	136–92[g]	–[b]	–[b]	10
HH	Sintering to Ag bridges	2	2.5 × 2.5 × 3	352	440	70[h]	1.6[e]	3.4[f]	This work
		4	2.5 × 2.5 × 3	400	510	62[h]	1.9[e]	3.1[f]	
		4	2.5 × 2.5 × 3	325	375	62[h]	1.04[e]	2.6[f]	

[a]At RT
[b]Not given
[c]For $N = 100$
[d]At 350°C
[e]Calculated using Eq. 1
[f]Calculated using Eq. 2
[g]After 500°C annealing
[h]At 63°C

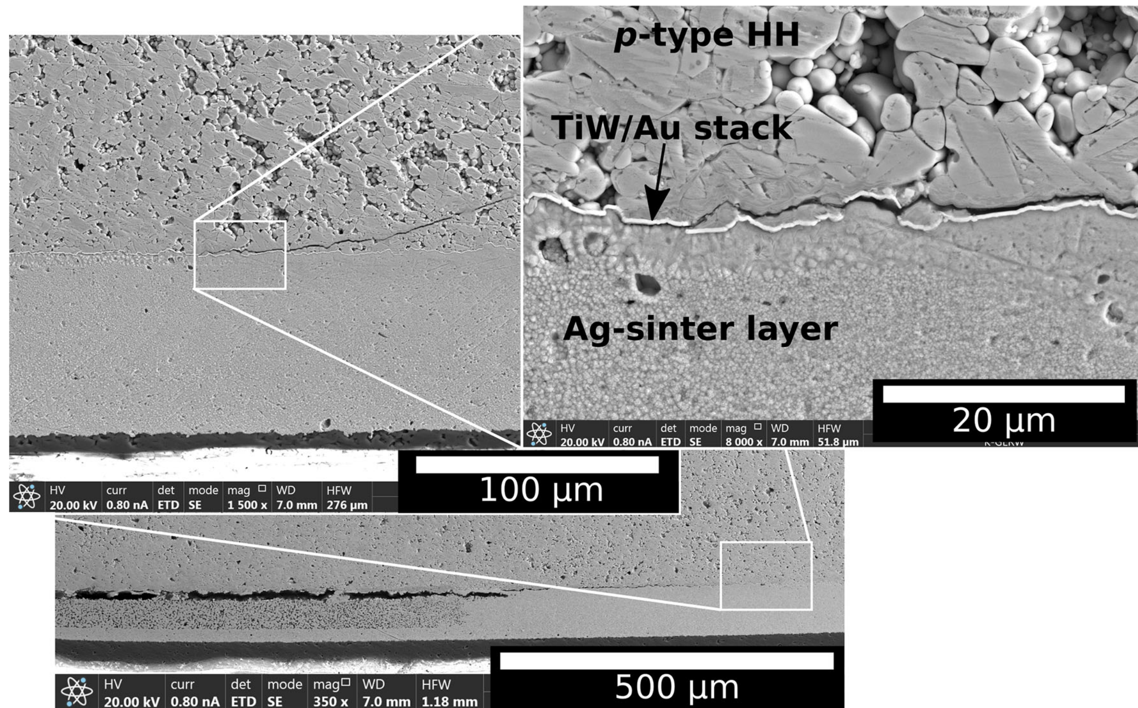

Fig. 11. SEM photograph of the cross section across the sinter-bonded interconnect of the hot side of a p-type $Hf_{0.5}Zr_{0.5}CoSn_{0.2}Sb_{0.8}$ leg. The corresponding four-leg TEG was operated up to 510°C.

were also neglected in the estimation of R_{th}. The overestimation of z_m caused by underestimating ΔT_{max} was therefore, to a certain degree, compensated for by the underestimated values of R_{th} (cf. Eq. 2). Moreover, as discussed above, the contributions of substrate and contact thermal resistances in our TE modules were rather low ($\sim$ 8% to $\sim$ 15% of R_{th} of the two-leg and the four-leg TEG, respectively). Deviations in this range may thus be expected for the z_m values of the sinter-bonded TEGs too.

The contact resistance of our device of $\rho_c \approx 60\ \mu\Omega cm^2$ to $100\ \mu\Omega\ cm^2$ versus $1\ \mu\Omega\ cm^2$ as assumed in[7] will be a main reason for the lower z_m. In this context, it should be noted that low values of $\rho_c \approx 1\ \mu\Omega\ cm^2$ can be also obtained with Ag-sintered interconnects. This was demonstrated with nanocrystalline silicon TEGs,[17] and should be strived also for the HHs by further improvement of the sinter parameters (pressure, temperature, time) and the surface roughness and morphology of the HH pellets. For a coherent full Heusler–HH interface, an ideal metal thermoelectric contact ($< 0.01\ \mu\Omega\ cm^2$) was predicted.[31]

After TE performance characterization, one of the four-leg modules was sectioned and prepared for cross-sectional SEM inspection. Figure 11 shows in three magnifications the hot-side interconnect of a p-$Hf_{0.5}Zr_{0.5}CoSn_{0.2}Sb_{0.8}$ leg with a homogeneous, densely sintered Ag layer in the right part of the lower figure (lowest magnification). Here, no interface is detectable between the sinter layer and the Ag pad layer on the ceramic plate. Towards the left side, the sinter layer has a larger porosity and had detached from the TE leg, which we assign to a too-low sintering pressure in this area. Inhomogeneous transfer of the pasty sinter powder and the open-pored surface topography of the TE legs may be responsible for the non-uniform pressure application.

Corresponding fracture patterns were found for the other legs on both hot-side and cold-side joints. In a higher magnified view of the densely sintered part of the joint (upper left figure), a crack can be detected extending from the interface between the sinter layer and the Au/TiW bilayer into deeper regions of the HH compound. The enlarged view depicted in the upper right figure shows that the crack line extends only over $\sim$ 15 μm along the interface between the sinter layer and Au/TiW metallization. Mostly, the crack runs above this interface through the HH compound, which indicates fracture in the HH pellet and corresponds to the top-view SEM damage patterns of broken one-leg TEGs after uniaxial tensile testing (cf. Fig. 8). Here, near-surface fracturing of the HH compound indicated by extended areas with detached fragments of HH material was considered as the prevalent reason for premature failure of our TEGs.

CONCLUSION AND OUTLOOK

We presented a fabrication process for TEGs based on HH compounds using the silver sinter-bonding method. A sputtered Au/TiW bilayer was employed as thin-film metallization and diffusion

barrier between the HH compounds and the metallization. Failure of the TEGs after uniaxial tensile-stress overloading revealed mixed fracture patterns of near-surface cracks in the HH compounds combined with adhesive failure between the sinter layer and the thin-film metallizations either on the TE leg or the ceramic substrate. After unintentional shock cooling of a TEG operated at high temperature, cracks were observed in the sinter layer. Temperature-dependent measurements of the internal resistance of two-leg and four-leg TE modules revealed a contact resistivity of 62 $\mu\Omega$ cm^2 to 70 $\mu\Omega$ cm^2 at 63°C. Seebeck voltage was measured at hot-side temperatures and temperature gradients (measured across the legs, i.e., temperature drops over the alumina substrates and their external heat contacts were not considered) up to 510°C and 400 K, respectively. Under these conditions, we obtained maximum power densities of 1.0 W cm^{-2} to 1.9 W cm^{-2} with two-leg and four-leg TEGs, respectively, and for the figure of merit of our devices, we estimated encouraging values of 2.6×10^{-4} K^{-1} (two-leg TEG) to 3.4×10^{-4} K^{-1} (four-leg TEG). Thus, despite the many challenges for improvement of stability and efficiency, the Ag sinter bonding technique can be a promising alternative for a cost-effective assembly of TE modules based on HH compounds. Nevertheless, optimization of the sinter bonding process including improved phase stability and smoother surface topography of the HH pellets as well as more homogeneous sinter paste transfer will be necessary to improve values of mechanical/thermal stability and contact resistance. Furthermore, performance testing of sinter-bonded HH-based TEGs over several days of operation, which was lacking so far, will be a forthcoming important issue.

ACKNOWLEDGMENTS

The authors gratefully acknowledge the support of the Department of Material Research of Volkswagen AG, Germany. We would also like to thank Mr. Dziony and Dr. Lilienkamp from the Institute of Energy Research and Physical Technologies (TU Clausthal) for the XPS measurements.

REFERENCES

1. K. Biswas, J. He, I.D. Blum, C.-I. Wu, T.P. Hogan, D.N. Seidman, V.P. Dravid, and M.G. Kanatzidis, *Nature* 489, 414 (2012).
2. S. LeBlanc, S.K. Yee, M.L. Scullin, C. Dames, and K.E. Goodson, *Renew. Sustain. Energy Rev.* 32, 313 (2014).
3. T. Kuroki, K. Kabeya, K. Makino, T. Kajihara, H. Kaibe, H. Hachiuma, H. Matsuno, and A. Fujibayashi, *J. Electron. Mater.* 43, 2405 (2014).
4. J. D'Angelo, E. Case, N. Matchanov, C. Wu, T. Hogan, J. Barnard, C. Cauchy, T. Hendricks, and M. Kanatzidis, *J. Electron. Mater.* 40, 10 (2011).
5. G. Schierning, R. Chavez, R. Schmechel, B. Balke, G. Rogl, and P. Rogl, *Trans. Mater. Res.* 2, 025001 (2015).
6. J.R. Salvador, J.Y. Cho, Z. Ye, J.E. Moczygemba, A.J. Thompson, J.W. Sharp, J.D. Koenig, R. Maloney, T. Thompson, J. Sakamoto, H. Wang, and A.A. Wereszczak, *Phys. Chem. Chem. Phys.* 16, 12510 (2014).
7. K. Bartholomé, B. Balke, D. Zuckermann, M. Köhne, M. Müller, K. Tarantik, and J. König, *J. Electron. Mater.* 43, 1775 (2014).
8. https://www.wassenberg-pr.de/wp-content/uploads/2018/06/PM_Isabellenh%C3%BCtte_Thermoelektrische-Abw%C3%A4rmeverstromung_180618.pdf. Accessed 10 May 2019.
9. J. Prado-Gonjal, M. Phillips, P. Vaqueiro, G. Min, A.V. Powell, and A.C.S. Appl, *Energy Mater.* 1, 6609 (2018).
10. B. Jayachandran, R. Gopalan, T. Dasgupta, and D. Sivaprahasam, *J. Electron. Mater.* 48, 1276 (2019).
11. P.H. Ngan, N. Van Nong, L.T. Hung, B. Balke, L. Han, E.M.J. Hedegaard, S. Linderoth, and N. Pryds, *J. Electron. Mater.* 45, 594 (2016).
12. G. Joshi and B. Poudel, *J. Electron. Mater.* 45, 6047 (2016).
13. J. Kähler, T. Kruspe, S. Jung, A. Stranz, A. Waag, and E. Peiner, *United States Patent Application* US 2012/0291454 A1; WO 2012/116107 A1; EP 2 810 310 A4.
14. J. Kähler, A. Stranz, A. Waag, and E. Peiner, *J. Electron. Mater.* 43, 2397 (2014).
15. A. Stranz, A. Waag, and E. Peiner, *J. Electron. Mater.* 44, 2055 (2015).
16. W. Wu, A. Bentaleb, A. Waag, and E. Peiner, *Mater. Today Proc.* 5, 10401 (2018).
17. V. Kessler, M. Dehnen, R. Chavez, M. Engenhorst, J. Stoetzel, N. Petermann, K. Hesse, T. Huelser, M. Spree, C. Stiewe, P. Ziolkowski, G. Schierning, and R. Schmechel, *J. Electron. Mater.* 43, 1389 (2014).
18. G. Schierning, H. Wiggers, and R. Schmechel, *ECS Trans.* 69, 3 (2015).
19. S.K. Bhagat, N.D. Theodore, and T.L. Alford, *Thin Solid Films* 516, 7451 (2008).
20. D. Zillmann, E. Peiner, A. Waag, A. Wolyniec, and M.-H. Feyand, *J. Electron. Mater.* 47, 1546 (2018).
21. N. Bundaleski, S. Petrović, D. Peruško, J. Kovač, and A. Zalar, *Appl. Surf. Sci.* 254, 6390 (2008).
22. A. Le Priol, L. Simonot, G. Abadias, P. Guérin, P.-O. Renault, and E. Le Bourhis, *Surf. Coat. Technol.* 237, 112 (2013).
23. F.Y. Xie, L. Gong, X. Liu, Y.T. Tao, W.H. Zhang, S.H. Chen, H. Meng, and J. Chen, *J. Electron. Spectrosc.* 185, 112 (2012).
24. J. Kähler, T. Kruspe, S. Jung, G. Palm, A. Stranz, A. Waag, and E. Peiner, *United States Patent Application* US 2012/0292009 A1.
25. J. Kähler, A. Stranz, A. Waag, and E. Peiner, *Oil Gas Eur. Mag.* 41, 38 (2015).
26. C.-C. Hsu and H.-K. Ma, *Mater. Sci. Eng., B* 198, 80 (2015).
27. M. Schaal, M. Klingler, and B. Wunderle, *Proceedings of 7th Electronic System-Integration Technology Conference (ESTC)*, Sept 18–21, 2018, Dresden, Germany.IEEE, 2018; https://doi.org/10.1109/estc.2018.8546498.
28. M. Yovanovich, J. Culham, and P. Teertstra, *Electron. Cooling* 3, 24 (1997).
29. J.R. Salvador, J.Y. Cho, Z. Ye, J.E. Moczygemba, A.J. Thompson, J.W. Sharp, J.D. König, R. Maloney, T. Thompson, J. Sakamoto, H. Wang, A.A. Wereszczak, and G.P. Meisner, *J. Electron. Mater.* 42, 1389 (2012).
30. S. Populoh, O.C. Brunko, K. Galazka, W. Xie, and A. Weidenkaff, *Materials* 6, 1326 (2013).
31. C.D. Spataru, Y. He, and F. Leonard, *APL Mater.* 7, 013202 (2019).

Publisher's Note Springer Nature remains neutral with regard to jurisdictional claims in published maps and institutional affiliations.